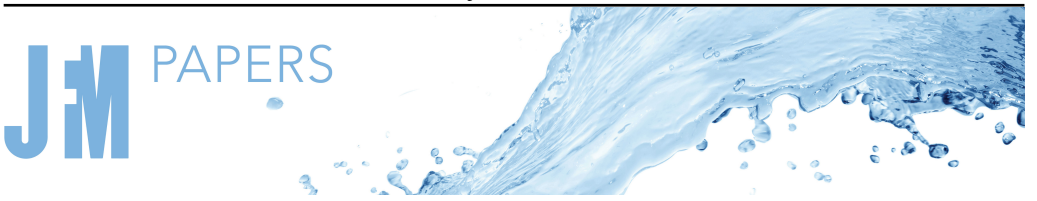
J. Fluid Mech. (2026), *vol.* 1029, A43, doi:10.1017/jfm.2026.11217



Depth-averaged and numerical modelling of magnetic fields induced by long surface gravity waves

Emiliano Renzi[1] **and Juliana Sartori Ziebell**[2]

[1]Mathematics of Complex and Nonlinear Phenomena (MCNP), School of Engineering, Physics and Mathematics, Northumbria University, Newcastle upon Tyne NE8 1ST, UK

[2]Departamento de Matemática Pura e Aplicada, Instituto de Matemática e Estatística, Universidade Federal do Rio Grande do Sul, Brazill

Corresponding author: Emiliano Renzi, emiliano.renzi@northumbria.ac.uk

(Received 21 August 2025; revised 11 November 2025; accepted 16 January 2026)

We derive a depth-averaged equation for the magnetic field induced by long surface gravity waves over variable seabed. The equation is verified using known analytical results and a novel numerical model for magnetic anomalies over variable bathymetry. Unlike amplitude-based theories, our results show that the magnetic response is governed by the forward energy flux associated with the surface gravity wave. This reframes the physics of long-wave magnetics and provides a new basis for interpreting geomagnetic observations.

Key words: geophysical and geological flows, shallow water flows, mathematical foundations

1. Introduction

Long surface gravity waves generate measurable anomalies in the Earth's magnetic field through the motion of conductive seawater across the geomagnetic field. These signals, detected by seafloor magnetometers and occasionally by low-Earth-orbit satellites, are attracting interest as a complementary tool for tsunami and storm-surge monitoring, see Toh *et al.* (2011), Wang & Liu (2013), Minami, Toh & Tyler (2015), Renzi & Mazza (2023) and references therein. Magnetic detection offers the possibility of inferring wave properties without relying solely on direct surface measurements.

Existing theoretical descriptions have focused almost exclusively on constant-depth domains. Tyler (2005) and Minami *et al.* (2015) derived closed-form expressions for the

© The Author(s), 2026. Published by Cambridge University Press. This is an Open Access article, distributed under the terms of the Creative Commons Attribution licence (https://creativecommons.org/licenses/by/4.0/), which permits unrestricted re-use, distribution and reproduction, provided the original article is properly cited.

https://doi.org/10.1017/jfm.2026.11217 Published online by Cambridge University Press

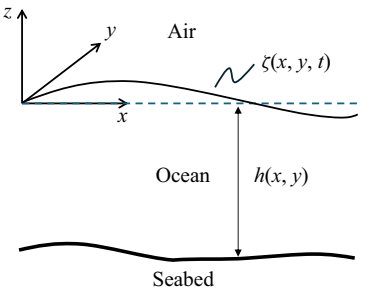


Figure 1. Schematic of the system's geometry.

magnetic field induced by progressive surface waves, showing proportionality between magnetic and free-surface amplitudes. This scaling holds for uniform depth h, but real waves propagate over variable bathymetry, where the wavenumber k varies, and shoaling, refraction and partial reflection occur. Fully numerical hydro-electromagnetic models, such as those of Minami & Toh (2013) and Minami *et al.* (2017), can reproduce these effects, but are computationally intensive, and typically impose artificial boundary conditions that force the magnetic field to vanish at the top and bottom of the computational box. Such constraints are inconsistent with the natural exponential decay of the field and can introduce spurious attenuation unless the vertical extent of the domain greatly exceeds the electromagnetic skin depth.

Here, we bridge this gap by deriving and testing a depth-averaged model for the magnetic field of long waves over slowly varying depth, supported by a new full numerical solution that eliminates box truncation by embedding the exact vertical decay structure analytically at the boundaries. This formulation combines asymptotic accuracy with numerical completeness: it reproduces constant-depth theory in the appropriate limit, captures bathymetric effects without artificial constraints, and isolates the fundamental coupling between hydrodynamic energy flux and electromagnetic induction.

Our results show that the induced magnetic field follows the propagation of wave energy rather than the local free-surface motion, revealing a flux-driven regime of long-wave magnetism that extends classical constant-depth theory to variable bathymetry.

The formulation places tsunami-generated magnetism within a broader class of coupled wave-field problems, where asymptotic analysis and direct simulation jointly expose the leading-order physics hidden from traditional finite-element approaches.

2. Governing equations

We consider a conductive ocean bounded above by air and below by an uneven seabed, as shown in figure 1. In three-dimensional space, let z be a vertical axis pointing upwards, orthogonal to the horizontal (x, y) plane, with $z = 0$ denoting the undisturbed ocean surface. The seabed is located at $z = -h(x, y)$ and $\zeta(x, y, t)$ represents the free-surface elevation, where t denotes time. We assume that the liquid is inviscid and incompressible and that the flow is irrotational (Mei, Stiassnie & Yue 2005).

Consider long waves, such as tsunamis, storm surges and tides, for which the free-surface amplitude A is much smaller than both the water depth h and the wavelength λ, and the shallow-water condition $\delta = kh \ll 1$ is satisfied, with $k = 2\pi/\lambda$ the wavenumber. The shallow-water approximation corresponds to the leading-order term of the full dispersion relation $\omega^2 = gk \tanh(kh)$, see Mei *et al.* (2005). For the long-wave regime considered here

https://doi.org/10.1017/jfm.2026.11217 Published online by Cambridge University Press

($kh \lesssim 0.3$), the dispersive correction $\tanh(kh)/(kh) - 1 \approx (kh)^2/3$ remains below 3 % and does not affect the leading-order dynamics.

The effect of the magnetic anomaly associated with such surface gravity waves on the oceanic flow field is negligible (Minami *et al.* 2015; Galtier 2016; Renzi & Mazza 2023). Hence, the surface gravity and electromagnetic problems are decoupled. Within the framework of linearised potential flow theory, the free-surface elevation satisfies the well-known long-wave equation

$$g\nabla \cdot (h\nabla \zeta) = \frac{\partial^2 \zeta}{\partial^2 t}, \tag{2.1}$$

where g is the acceleration due to gravity. The scattered waves generated by the interaction of incident waves with the seabed must be outgoing in the far field as $|\boldsymbol{x}| = |(x, y)| \to \infty$ (Mei *et al.* 2005). We now turn to the magnetic field.

Consider a conductive medium moving with velocity $\boldsymbol{u}$ and characterised by a magnetic diffusivity $\eta = (\mu_0 \sigma)^{-1}$, where μ_0 is the permeability of free space and σ is the electrical conductivity (Minami *et al.* 2015). Within the framework of kinematic dynamo theory, the magnetic anomaly $\boldsymbol{b}(\boldsymbol{x}, z, t)$ must satisfy the advection–diffusion equation

$$\frac{\partial \boldsymbol{b}}{\partial t} = \boldsymbol{F} \cdot \nabla \boldsymbol{u} - \boldsymbol{F} \nabla \cdot \boldsymbol{u} + \eta \nabla^2 \boldsymbol{b}, \tag{2.2}$$

where $\boldsymbol{F}$ is the steady Earth's field, see Davidson (2016). In the liquid region $\Omega_L = \{\boldsymbol{x} \in \mathbb{R}^2, -h < z < 0\}$, the magnetic anomaly satisfies (2.2) with $\boldsymbol{u}$ being the velocity field induced by the long wave (2.1). A similar equation must be satisfied in the air region $\Omega_A = \{\boldsymbol{x} \in \mathbb{R}^2, z > 0\}$ and the seabed region $\Omega_S = \{\boldsymbol{x} \in \mathbb{R}^2, z < -h\}$, where $\boldsymbol{u} = \boldsymbol{0}$. Since the electrical conductivity in both air and soil is much lower than that of seawater (Wang & Liu 2013), we consider the limit $\eta \to \infty$ for insulating media, such that (2.2) becomes

$$\nabla^2 \boldsymbol{b} = 0 \tag{2.3}$$

for $(\boldsymbol{x}, z) \in \Omega_A \cup \Omega_s$. The small electrical conductivity of the seabed would introduce errors of only a few percent (Minami *et al.* 2015), which can be reasonably neglected (Wang & Liu 2013; Tatehata, Ichihara & Hamano 2015; Renzi & Mazza 2023). Finally, we require the magnetic field to remain bounded as $|z| \to \infty$ and to be continuous at the air–ocean ($z = 0$) and ocean–seabed ($z = -h$) interfaces (Moreau 1990; Tyler 2005; Wang & Liu 2013).

In the following, we first revisit the solution for constant depth, which will be instrumental in obtaining a novel depth-averaged equation for the magnetic field over a variable seabed.

3. Solution for constant depth

The analysis assumes an inviscid fluid and an electrically insulating seabed, which is appropriate for long-wave conditions where viscous losses and sub-bottom induction are small compared with the free-surface and bulk conductive responses (Wang & Liu 2013). Finite bottom conductivity or hydrodynamic friction would mainly introduce small amplitude damping without altering the flux-governed coupling mechanism described later.

3.1. *Wave field*

Consider a narrow-banded approach, with harmonic motion of frequency ω, such that

$$\zeta(\boldsymbol{x}, t) = \mathrm{Re}\{\Theta(\boldsymbol{x})\ \exp(-\mathrm{i}\omega t)\}, \tag{3.1}$$

https://doi.org/10.1017/jfm.2026.11217 Published online by Cambridge University Press

where the real part will be omitted from now on for the sake of brevity. Substituting (3.1) into the governing long-wave equation (2.1) and applying separation of variables yields the well-known solution

$$\Theta(\boldsymbol{x}) = A_0 \exp(\mathrm{i}\boldsymbol{k}\cdot\boldsymbol{x}), \tag{3.2}$$

where A_0 is the constant wave amplitude and $\boldsymbol{k} = (k_x, k_y)$ is the wavenumber satisfying the dispersion relation $\omega = k\sqrt{gh}$, with $k = |\boldsymbol{k}|$, see Mei *et al.* (2005). The velocity field is given by $\boldsymbol{u}(\boldsymbol{x}, z, t) = \boldsymbol{v}(\boldsymbol{x}, z)\exp(-\mathrm{i}\omega t)$, where the spatial component

$$\boldsymbol{v} = -\frac{\mathrm{i}g}{\omega}\nabla\Theta = \frac{g}{\omega}\boldsymbol{k}\,\Theta. \tag{3.3}$$

3.2. *Magnetic field*

We focus on the vertical component of the magnetic field, as it has promising potential for early-warning applications (Wang & Liu 2013; Renzi & Mazza 2023). Similar calculations can be performed for the horizontal components, but we do not present them here. However, they can be derived by following the same steps. The magnetic field is

$$\boldsymbol{b}(\boldsymbol{x}, z, t) = \boldsymbol{\beta}(\boldsymbol{x}, z)\exp(-\mathrm{i}\omega t), \tag{3.4}$$

with $\boldsymbol{\beta} = (\beta_x, \beta_y, \beta_z)$. Substituting (3.4) into the governing equation (2.2) and taking the vertical component yields

$$\nabla^2\beta_z + \frac{\mathrm{i}\omega}{\eta}\beta_z = -\frac{\mathrm{i}gF_z}{\omega\eta}\nabla^2\Theta, \quad (\boldsymbol{x}, z) \in \Omega_L, \tag{3.5}$$

where subscripts denote the respective scalar components. Similarly, (2.3) becomes

$$\nabla^2\beta_z = 0, \quad (\boldsymbol{x}, z) \in \Omega_A \cup \Omega_S. \tag{3.6}$$

Separation of variables and variation of parameters, together with continuity of β_z and $\partial\beta_z/\partial z$ at the common boundaries $z = 0$ and $z = -h$ (Tyler 2005; Wang & Liu 2013; Renzi & Mazza 2023) yield the full solution

$$\beta_z(\boldsymbol{x}, z) = f(z)\Theta(\boldsymbol{x}), \tag{3.7}$$

where

$$f(z) = -\frac{\mathrm{i}gF_zk^2}{\alpha^2\omega\eta}\frac{\alpha\sinh(\alpha h/2)}{k\cosh(\alpha h/2) + \alpha\sinh(\alpha h/2)}\exp(-kz), \quad z \geqslant 0, \tag{3.8}$$

$$f(z) = -\frac{\mathrm{i}gF_zk^2}{\alpha^2\omega\eta}\frac{k\cosh(\alpha h/2) - k\cosh[(h+2z)\alpha/2] + \alpha\sinh(\alpha h/2)}{k\cosh(\alpha h/2) + \alpha\sinh(\alpha h/2)}, \quad -h \leqslant z \leqslant 0, \tag{3.9}$$

$$f(z) = -\frac{\mathrm{i}gF_zk^2}{\alpha^2\omega\eta}\frac{\alpha\sinh(\alpha h/2)}{k\cosh(\alpha h/2) + \alpha\sinh(\alpha h/2)}\exp\left[k(z+h)\right], \quad z \leqslant -h. \tag{3.10}$$

In the latter, $\alpha = \sqrt{k^2 - \mathrm{i}\omega/\eta}$ is the complex magnetic wavenumber (Minami *et al.* 2015), with the principal value of the square root taken using a branch cut along the negative real axis. Note that $f(z)$ is $\mathrm{C}^1(\mathbb{R})$ to satisfy the continuity conditions at the air–liquid and liquid–soil interfaces, and $f \to 0$ exponentially as $|z| \to \infty$. In the limit $kh \to 0$, (3.7) and

https://doi.org/10.1017/jfm.2026.11217 Published online by Cambridge University Press

(3.9) together yield

$$\frac{\beta_z}{F_z} = \frac{\sqrt{gh}}{h\sqrt{gh} + 2\mathrm{i}\eta}\Theta, \tag{3.11}$$

which is identical to the constant-depth expression of Tyler (2005) (see also Renzi & Mazza 2023). Although derived for uniform depth, this amplitude law is often applied locally by replacing $h \to h(x)$ (e.g. Tyler 2005; Minami *et al.* 2015); we assess the validity of that *ad hoc* extension in § 7.

Substitution of (3.7) into (3.5) and (3.6) reveals that f satisfies

$$\frac{\partial^2 f}{\partial z^2} - \alpha^2 f = \frac{\mathrm{i}F_z g k^2}{\omega\eta}, \quad (\boldsymbol{x}, z) \in \Omega_L, \tag{3.12}$$

and

$$\frac{\partial^2 f}{\partial z^2} - k^2 f = 0, \quad (\boldsymbol{x}, z) \in \Omega_A \cup \Omega_S, \tag{3.13}$$

which can be readily verified using (3.8)–(3.10). We now derive a depth-averaged equation for the vertical magnetic field over variable depth.

4. Depth-averaged equation for the magnetic field

We consider slowly varying bathymetry such that $\epsilon = |\nabla h|/(kh) \ll 1$. While the long-wave parameter $\delta = kh$ controls the vertical structure, ϵ governs the horizontal modulation. In the mild-slope limit, we assume that the vertical structure of the magnetic field remains that of the constant-depth solution f given by (3.8)–(3.10), with only a weak, parametric dependence on the local depth $h(\boldsymbol{x})$. Accordingly, we seek a separable solution of the form

$$\beta_z(\boldsymbol{x}, z) = f(z,\ h(\boldsymbol{x}))\ \ X(\boldsymbol{x}), \tag{4.1}$$

where $X(\boldsymbol{x})$ varies on the slow horizontal scale $O(1/\epsilon)$. The governing equations (3.5)–(3.6) are valid for variable depth; however, we now rewrite them as

$$\frac{\partial^2 \beta_z}{\partial z^2} + \nabla_2^2 \beta_z + \frac{\mathrm{i}\omega}{\eta}\beta_z = -\frac{\mathrm{i}g F_z}{\omega\eta}\nabla_2^2\Theta, \quad (\boldsymbol{x}, z) \in \Omega_L, \tag{4.2}$$

and

$$\frac{\partial^2 \beta_z}{\partial z^2} + \nabla_2^2 \beta_z = 0, \quad (\boldsymbol{x}, z) \in \Omega_A \cup \Omega_S, \tag{4.3}$$

respectively, where $\nabla_2 = (\partial/\partial x, \partial/\partial y)$ is the horizontal gradient. We also request that β_z be finite as $|z| \to \infty$.

Now, regard (4.2)–(4.3) as ordinary differential equations in z and apply Green's second identity separately in each region, using (3.12)–(3.13) for f, so that

$$\int_{-\infty}^{-h} \left(f(-\nabla_2^2 \beta_z) - \beta_z k^2 f \right) \mathrm{d}z = \left[f\frac{\partial \beta_z}{\partial z} - \beta_z \frac{\partial f}{\partial z} \right]_{z=-h}, \tag{4.4}$$

$$\int_{-h}^{0} \left[f\left(-\nabla_2^2 \beta_z - \frac{\mathrm{i}\omega}{\eta}\beta_z - \frac{\mathrm{i}g F_z}{\omega\eta}\nabla_2^2\Theta \right) - \beta_z \left(\alpha^2 f + \frac{\mathrm{i}F_z g k^2}{\omega\eta} \right) \right] \mathrm{d}z$$

$$= \left[f\frac{\partial \beta_z}{\partial z} - \beta_z \frac{\partial f}{\partial z} \right]_{z=-h}^{z=0} \tag{4.5}$$

https://doi.org/10.1017/jfm.2026.11217 Published online by Cambridge University Press

and

$$\int_0^\infty \left(f(-\nabla_2^2 \beta_z) - \beta_z k^2 f \right) \mathrm{d}z = -\left[f \frac{\partial \beta_z}{\partial z} - \beta_z \frac{\partial f}{\partial z} \right]_{z=0}. \tag{4.6}$$

Using (4.1), the horizontal Laplacian becomes

$$\nabla_2^2 \beta_z = f \nabla_2^2 X + 2 \frac{\partial f}{\partial h} \boldsymbol{\nabla}_2 X \cdot \boldsymbol{\nabla}_2 h + X \frac{\partial^2 f}{\partial h^2} (\boldsymbol{\nabla}_2 h)^2 + X \frac{\partial f}{\partial h} \nabla_2^2 h. \tag{4.7}$$

Consider the depth-averaged integral (4.5) for the liquid layer. Substituting (3.7), (4.7) in (4.5) and using (4.4), (4.6) as boundary conditions at $z = -h$ and $z = 0$, respectively, yields

$$\begin{aligned}
&\nabla_2^2 X \int_{-h}^0 f^2 \,\mathrm{d}z + 2\boldsymbol{\nabla}_2 X \cdot \boldsymbol{\nabla}_2 h \int_{-h}^0 f \frac{\partial f}{\partial h} \,\mathrm{d}z + X \int_{-h}^0 f \frac{\partial^2 f}{\partial h^2} \,\mathrm{d}z \, (\boldsymbol{\nabla}_2 h)^2 \\
&+ X \int_{-h}^0 f \frac{\partial f}{\partial h} \,\mathrm{d}z \, \nabla_2^2 h + \frac{\mathrm{i}\omega}{\eta} X \int_{-h}^0 f^2 \,\mathrm{d}z + \frac{\mathrm{i} F_z g}{\omega \eta} \nabla_2^2 \Theta \int_{-h}^0 f \,\mathrm{d}z + X\alpha^2 \int_{-h}^0 f^2 \,\mathrm{d}z \\
&+ X \frac{\mathrm{i} F_z g k^2}{\omega \eta} \int_{-h}^0 f \,\mathrm{d}z = -\nabla_2^2 X \int_0^{+\infty} f^2 \,\mathrm{d}z - 2\boldsymbol{\nabla}_2 X \cdot \boldsymbol{\nabla}_2 h \int_0^{+\infty} f \frac{\partial f}{\partial h} \,\mathrm{d}z \\
&- X \int_0^{+\infty} f \frac{\partial^2 f}{\partial h^2} \,\mathrm{d}z \, (\boldsymbol{\nabla}_2 h)^2 - X \int_0^{+\infty} f \frac{\partial f}{\partial h} \,\mathrm{d}z \, \nabla_2^2 h - Xk^2 \int_0^{+\infty} f^2 \,\mathrm{d}z \\
&- \nabla_2^2 X \int_{-\infty}^{-h} f^2 \,\mathrm{d}z - 2\boldsymbol{\nabla}_2 X \cdot \boldsymbol{\nabla}_2 h \int_{-\infty}^{-h} f \frac{\partial f}{\partial h} \,\mathrm{d}z - X \int_{-\infty}^{-h} f \frac{\partial^2 f}{\partial h^2} \,\mathrm{d}z \, (\boldsymbol{\nabla}_2 h)^2 \\
&- X \int_{-\infty}^{-h} f \frac{\partial f}{\partial h} \,\mathrm{d}z \, \nabla_2^2 h - Xk^2 \int_{-\infty}^{-h} f^2 \,\mathrm{d}z.
\end{aligned} \tag{4.8}$$

Collecting terms proportional to $\nabla_2^2 X$, $\boldsymbol{\nabla}_2 X \cdot \boldsymbol{\nabla}_2 h$ and X, and recalling that f in (3.8)–(3.10) is integrable over the full domain $z \in \mathbb{R}$, (4.8) simplifies into

$$\begin{aligned}
&\nabla_2^2 X \int_{-\infty}^{+\infty} f^2 \,\mathrm{d}z + 2\boldsymbol{\nabla}_2 X \cdot \boldsymbol{\nabla}_2 h \int_{-\infty}^{+\infty} f \frac{\partial f}{\partial h} \,\mathrm{d}z + k^2 X \int_{-\infty}^{+\infty} f^2 \,\mathrm{d}z \\
&\qquad + \frac{\mathrm{i} g F_z}{\omega \eta} \left(k^2 X + \nabla_2^2 \Theta \right) \int_{-h}^0 f \,\mathrm{d}z = O\big((\nabla_2 h)^2\big) + O\big(\nabla_2^2 h\big),
\end{aligned} \tag{4.9}$$

where the integrals can be calculated analytically, as detailed in Appendix A.

Equation (4.9) represents the electromagnetic analogue of the classical mild-slope equation in the long-wave limit. It governs the slowly varying horizontal amplitude $X(\boldsymbol{x})$ of the vertical magnetic field β_z (3.7) within the liquid layer Ω_L, induced by the long-wave potential $\Theta(\boldsymbol{x})$ over a gently varying seabed.

Under the long-wave and mild-slope assumptions, $\delta = kh \ll 1$ and $\epsilon = |\boldsymbol{\nabla}_2 h|/(kh) \ll 1$, and hence, $|\boldsymbol{\nabla}_2 h| \ll \delta \ll 1$. The terms proportional to ∇_2^2 and to k^2 on the left-hand side of (4.9) are $O(\delta^2)$, and provide the leading contribution. The mixed topographic term $\boldsymbol{\nabla}_2 X \cdot \boldsymbol{\nabla}_2 h$ is $O(\epsilon\,\delta^2)$ and introduces the slow horizontal modulation. By contrast, the slope-squared and curvature remainders, $(\boldsymbol{\nabla}_2 h)^2$ and $\nabla_2^2 h$, scale as $O(\epsilon^2 \delta^2)$ and are therefore neglected at the present order. Accordingly, we retain terms up to $O(\epsilon\,\delta^2)$ in what follows.

https://doi.org/10.1017/jfm.2026.11217 Published online by Cambridge University Press

4.1. *Mild-slope form of the depth-integrated equation*

For a generic depth $h(x, y)$, we define the depth-integrated coefficients associated with the electromagnetic vertical mode $f(z, h)$ as

$$A(h) = \int_{-\infty}^{\infty} f^2 \, \mathrm{d}z, \qquad B(h) = \int_{-\infty}^{\infty} f \, \frac{\partial f}{\partial h} \, \mathrm{d}z, \qquad C(h) = \int_{-h}^{0} f \, \mathrm{d}z, \tag{4.10}$$

which satisfy the exact differential identity

$$\frac{\mathrm{d}A}{\mathrm{d}h} = 2B. \tag{4.11}$$

Here, A measures the vertical magnetic energy density, B controls the first-order coupling with bottom slope and C controls the electromagnetic coupling through $\nabla_2^2 \Theta$.

Equation (4.9) can then be expressed in the mild-slope form

$$\boldsymbol{\nabla}_2 \cdot \big(A(h)\, \boldsymbol{\nabla}_2 X\big) + A(h)\, k^2 (1 + r)\, X = -A(h) r \nabla_2^2 \Theta, \qquad r = \frac{igF_z}{\omega \eta} \frac{C}{A}, \tag{4.12}$$

which is formally analogous to Berkhoff's mild-slope equation for surface gravity waves (Mei *et al.* 2005). Both equations describe the lateral propagation of a depth-modulated mode governed by a weighting coefficient, but they differ in physical interpretation. In Berkhoff's theory, the unknown is the free-surface elevation and the weight $a = cC_g$ (with c being the phase speed and C_g the group speed) arises from wave-action conservation. Here, by contrast, the unknown X represents the electromagnetic field induced by the moving surface and $A(h)$ originates from the vertical mode $f(z, h)$, measuring the magnetic energy stored in the system. Finally, the complex coupling r introduces magnetic diffusion, breaking the self-adjoint character of Berkhoff's operator.

5. Numerical solution

Existing numerical models of tsunami-generated electromagnetic fields, such as the finite-element formulations of Minami & Toh (2013) and Minami *et al.* (2017), solve the induction equations in a finite domain under Dirichlet-type boundary conditions that force the magnetic field to vanish at the top and bottom boundaries of the computational domain. Although acceptable for sufficiently large domains, this treatment does not reproduce the true exponential decay of the field and may introduce artificial attenuation unless the domain height greatly exceeds the electromagnetic skin depth. The analytical framework introduced in § 3 embeds the correct vertical structure of the field, eliminating the need for artificial boundaries and providing the basis for a more computationally efficient and physically consistent solution.

5.1. *Formulation*

We construct a full numerical model based on a step approximation of the wave and electromagnetic fields. This procedure coincides algebraically with the transition-matrix formalism of Devillard, Dunlop & Souillard (1988) and with the generalised version of Evans & Linton (1994). Here, the discretisation is applied directly to the bathymetry, making it a projection of the full operator onto a piecewise-constant (Haar) subspace in the physical plane. While the approach itself is not new, to our knowledge, this is the first time it has been applied to the magnetic field in the context of wave-induced electromagnetism.

This formulation is two-dimensional in the (x, z) plane; an extension to fully three-dimensional (3-D) bathymetries can be obtained by applying the same step-wise matching

https://doi.org/10.1017/jfm.2026.11217 Published online by Cambridge University Press

procedure independently in the transverse direction, leading to coupled 3-D transfer relations.

We seek a time-harmonic solution $\zeta(x,t) = \mathrm{Re}\{\Theta(x)\,\mathrm{e}^{-i\omega t}\}$, which gives the scalar ordinary differential equation (ODE)

$$\big(h(x)\,\Theta'\big)' + \frac{\omega^2}{g}\,\Theta = 0, \tag{5.1}$$

where primes denote differentiation and the bathymetry smoothly connects to constant-depth regions as $x \to \pm\infty$, where standard radiation conditions are imposed (Mei *et al.* 2005).

5.2. *Step approximation and Haar projection*

To obtain a tractable full numerical solution without slope assumptions, the bottom profile is replaced by a piecewise-constant function

$$h(x) \approx \sum_{j=1}^{N} h_j\,\chi_j(x), \qquad \chi_j(x) = \begin{cases} 1, & x_{j-1} < x < x_j, \\ 0, & \text{otherwise}, \end{cases} \qquad j = 1,\ldots,N. \tag{5.2}$$

The functions $\chi_j(x)$ form a Haar-type basis. Projecting (5.1) onto this subspace yields, on each strip j,

$$\Theta'' + k_j^2\,\Theta = 0, \qquad k_j^2 = \frac{\omega^2}{g h_j}, \qquad x_{j-1} < x < x_j, \tag{5.3}$$

whose general solution is

$$\Theta_j(x) = T_j\,\exp\big(\mathrm{i}k_j x\big) + R_j\,\exp\big(-\mathrm{i}k_j x\big), \tag{5.4}$$

where T_j and R_j are unknown complex values. The computational domain is truncated at $x_0 = x_L$ on the left and $x_{N+1} = x_R$ on the right, representing the constant-depth regions as $x \to \pm\infty$. Boundary conditions are imposed by prescribing a unit incident amplitude from the left ($T_0 = 1$) and no incoming wave from the right ($R_{N+1} = 0$).

At each step $x = x_j$, we enforce

$$\Theta_j = \Theta_{j+1}, \qquad h_j\,\Theta_j' = h_{j+1}\,\Theta_{j+1}', \tag{5.5}$$

i.e. continuity of surface elevation and mass flux. This yields a system of $2N+2$ equations in as many unknowns,

$$T_j\,\exp\big(\mathrm{i}k_j x_j\big) + R_j\,\exp\big(-\mathrm{i}k_j x_j\big) - T_{j+1}\,\exp\big(\mathrm{i}k_{j+1} x_j\big) - R_{j+1}\exp\big(-\mathrm{i}k_{j+1} x_j\big) = 0, \tag{5.6}$$

$$T_j \mathrm{i}k_j h_j \exp\big(\mathrm{i}k_j x_j\big) - R_j \mathrm{i}k_j h_j \exp\big(-\mathrm{i}k_j x_j\big) - T_{j+1}\mathrm{i}k_{j+1}h_{j+1}\exp\big(\mathrm{i}k_{j+1}x_j\big) + R_{j+1}\mathrm{i}k_{j+1}h_{j+1}\exp\big(-\mathrm{i}k_{j+1}x_j\big) = 0. \tag{5.7}$$

Energy conservation requires

$$E = |R_0|^2 + \sqrt{\frac{h_R}{h_L}}\,|T_{N+1}|^2 = 1, \tag{5.8}$$

and deviations of E from unity provide a convergence diagnostic.

https://doi.org/10.1017/jfm.2026.11217 Published online by Cambridge University Press

The magnetic field is obtained by applying, on each constant-depth strip, the exact linear constant-depth transfer relation

$$\beta_{z_j}(x) = f_j(-h_j)\,\Theta_j(x), \tag{5.9}$$

where f_j denotes the Haar projection of (3.8)–(3.10) and embeds the electromagnetic coupling for depth h_j. This represents a quasi-local induction approximation, as the vertical electromagnetic structure is solved exactly within each strip, while lateral coupling between adjacent strips is neglected. The approach is asymptotically valid when

$$\Delta x = x_{j+1} - x_j \ll \min\big(\lambda,\ \delta_{EM}\big), \qquad \delta_{EM} = \sqrt{\frac{2\eta}{\omega}}, \tag{5.10}$$

so that both the hydrodynamic wavelength λ and the electromagnetic skin depth δ_{EM} exceed the strip width. No depth-integrated or mild-slope separation is invoked in this formulation, which therefore constitutes a fully numerical solution.

6. Model implementation and validation

6.1. *Depth-averaged model*

6.1.1. *General approach*

Equation (4.9) is solved numerically for prescribed bathymetric profiles $h(\boldsymbol{x})$. In the present work, we focus on parallel depth contours $h = h(x)$. The depth-averaged (4.9) becomes

$$L(X) = X'' + h' p(h(x))X' + q(h(x))X + r(h(x))\Theta'' = 0, \tag{6.1}$$

where primes denote differentiation with respect to x and

$$p(h(x)) = \frac{2B}{A};\ q(h(x)) = k^2(1 + r(h(x)). \tag{6.2}$$

The latter expressions depend on the electromagnetic structure through $f(z)$ and have analytical expressions upon substitution of (A1)–(A3). Boundary conditions depend on the particular geometry being investigated and are detailed in the validation § 6.3.

6.1.2. *Treatment of slope discontinuities*

Canonical piecewise-linear bottom profiles, consisting of flat regions connected by planar slopes, have been widely employed in the study of coastal and tsunami wave propagation (e.g. Dingemans 1997; Sammarco *et al.* 2013; Abdolali, Kirby & Bellotti 2015). In such configurations, the bottom derivative h' is discontinuous at a junction x_c and, therefore, must be handled carefully within the depth-integrated framework. This is because the step discontinuity in h' at x_c introduces distributional terms $h'' \propto \delta(x - x_c)$, which make the contribution from the $O(\nabla_2^2 h)$ terms in (4.9) non-negligible.

Consider the governing equation (4.8) and retain the terms $O(\nabla_2^2 h)$ on the right-hand side,

$$\text{right-hand side} = -XB\nabla_2^2 h. \tag{6.3}$$

Writing again the equation in conservative form, considering the two-dimensional limit and integrating across an infinitesimal control volume surrounding a junction point x_c yields the formal jump condition

$$\big[A(h)X'\big] = -\,B(h)[h']X. \tag{6.4}$$

https://doi.org/10.1017/jfm.2026.11217 Published online by Cambridge University Press

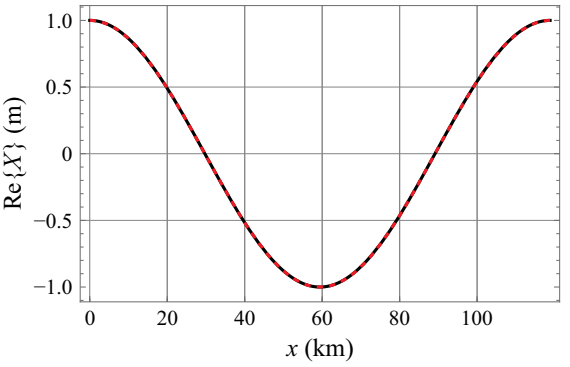


Figure 2. Plot of $\mathrm{Re}\{X(x)\}$ for constant depth $h = 4000$ m, obtained with the numerical solution (- -) of the depth-averaged (6.1) and the analytical solution (- -), for $t = 600$ s and $A_0 = 1$ m.

In the latter expression, $[f]$ denotes the jump of $f(x)$ across x_c. Using (4.10), the jump condition (6.4) becomes

$$X'(x_c^+) = X'(x_c^-) - \frac{p(x_c)}{2}\Delta h'(x_c)X(x_c), \tag{6.5}$$

where $\Delta h'(x_c)$ is the jump in steepness at x_c. This Rankine–Hugoniot-type condition ensures conservation of the depth-integrated electromagnetic flux across the slope breaks while maintaining continuity of the field X. In the numerical implementation, the jump is imposed explicitly at a discontinuity point x_c through a local update of X', which reproduces the finite discontinuity predicted by the asymptotic theory and avoids spurious reflections. As $\Delta h' \to 0$, (6.5) recovers the smooth mild-slope limit.

6.2. *Full numerical model*

The numerical implementation assembles the matrix (5.6)–(5.7), solves for the coefficients (T_j, R_j) using sparse linear algebra, and reconstructs the free-surface elevation and derived quantities (e.g. magnetic perturbations) along the domain. Increasing the number of steps N results in converged solutions, with the total energy balance satisfied to excellent precision $O(10^{-14})$, see Appendix B.

6.3. *Validation of the depth-averaged model*

6.3.1. *Analytical validation*

First, we consider the case of constant depth, $h = h_0$, for which $\Theta = A_0 \exp(\mathrm{i}kx)$. The depth-averaged (6.1) is solved numerically using periodic boundary conditions, i.e. $X(0) = X(\lambda)$, where $\lambda = 2\pi/k$. The numerical solution is obtained with Mathematica(R) using an explicit Runge–Kutta scheme of order 8. The computational time on an Intel(R) Core(TM) i7-10700 machine equipped with a 2.90 GHz CPU and 64 GB RAM is $O(2\ \mathrm{s})$. Figure 2 shows the behaviour of $X(x)$ over a wavelength, compared with the analytical solution for constant depth obtained in § 3. Parameters are $h = 4000$ m, $F_z = -20\,000$ nT, $\eta = 198\,944\ \mathrm{m^2\ s^{-1}}$ and a period of 600 s. The numerical and analytical curves are visually indistinguishable. We quantify the agreement using the relative L_2 norm,

$$L_2 = \frac{||X_{num} - X_{ana}||_2}{||X_{ana}||_2}, \tag{6.6}$$

https://doi.org/10.1017/jfm.2026.11217 Published online by Cambridge University Press

which measures the root-mean-square (r.m.s) difference, and the relative infinity norm,

$$L_\infty = \frac{\max |X_{num} - X_{ana}|}{\max |X_{ana}|}, \tag{6.7}$$

which measures the worst pointwise error, where X_{num} and X_{ana} represent the numerical and analytical solutions, respectively (Miller, Renzi & Discacciati 2025). We have $L_2 = 4.9 \times 10^{-9}$ and $L_\infty = 2.2 \times 10^{-8}$ providing robust validation of (4.9) in the case of constant depth.

6.3.2. *Numerical validation*

We now validate the depth-integrated model against the full numerical model for varying bathymetry. As a commonly used benchmark test (Sammarco *et al.* 2013; Abdolali *et al.* 2015), we examine a configuration consisting of two regions of constant depth connected by a sloping transition. The water depth is $h = h_0$ for $x < 0$ and $h = h_1$ for $x > x_1$, while in the transition region of variable depth, it is given by $h = h_0 - mx$, ensuring that $h_1 = h_0 - mx_1$.

The wave field admits an analytical solution, found by solving the wave equation (2.1) separately in each region, and matching pressure and fluxes at the common boundaries at $x = 0$ and $x = x_1$. This yields

$$\Theta = \exp(\mathrm{i}k_0 x) + R\exp(-\mathrm{i}k_0 x), \quad x < 0, \tag{6.8}$$

$$\Theta = R_0 J_0\left(2\sqrt{s(h_0 - mx)}\right) + T_0 Y_0\left(2\sqrt{s(h_0 - mx)}\right), \quad 0 < x < x_1, \tag{6.9}$$

$$\Theta = T\exp(\mathrm{i}k_1(x - x_1)), \quad x > x_1, \tag{6.10}$$

where $k_{(0,1)} = \omega/\sqrt{gh_{(0,1)}}$, $s = \omega^2/(m^2 g)$ and J_0, Y_0 are respectively the Bessel functions of first and second kind and order zero. Still in (6.8)–(6.10),

$$R_0 = \frac{2k_0(Q_1 - \mathrm{i}k_1 Y_{0,1})}{Q_1(J_{0,0}k_0 - \mathrm{i}S_0) + (J_{0,1}k_1 + \mathrm{i}S_1)(Q_0 + \mathrm{i}k_0 Y_{0,0}) - k_1 Y_{0,1}(S_0 + \mathrm{i}J_{0,0}k_0)}, \tag{6.11}$$

$$T_0 = \frac{2k_0(J_{0,1}k_1 + \mathrm{i}S_1)}{Q_1(-S_0 - \mathrm{i}J_{00}k_0) + (S_1 - \mathrm{i}J_{0,1}k_1)(Q_0 + \mathrm{i}k_0 Y_{0,0}) + k_1 Y_{0,1}(-J_{0,0}k_0 + \mathrm{i}S_0)}, \tag{6.12}$$

$$R = \frac{k_1 Y_{0,1}(J_{0,0}k_0 + \mathrm{i}S_0) + (-S_0 + \mathrm{i}J_{0,0}k_0)Q_1 + (S_1 - \mathrm{i}J_{0,1}k_1)(Q_0 - \mathrm{i}k_0 Y_{0,0})}{Q_1(S_0 + \mathrm{i}J_{0,0}k_0) + \mathrm{i}(J_{0,1}k_1 + \mathrm{i}S_1)(Q_0 + \mathrm{i}k_0 Y_{0,0}) + k_1 Y_{0,1}(J_{0,0}k_0 - \mathrm{i}S_0)}, \tag{6.13}$$

$$T = \frac{2k_0(J_{0,1}Q_1 - S_1 Y_{0,1})}{Q_1(J_{0,0}k_0 - \mathrm{i}S_0) + (J_{0,1}k_1 + \mathrm{i}S_1)(Q_0 + \mathrm{i}k_0 Y_{0,0}) - k_1 Y_{0,1}(S_0 + \mathrm{i}J_{0,0}k_0)}, \tag{6.14}$$

where $J_{0,0} = J_0(2\sqrt{sh_0})$, $J_{0,1} = J_0(2\sqrt{sh_1})$, $Y_{0,0} = Y_0(2\sqrt{sh_0})$, $Y_{0,1} = Y_0(2\sqrt{sh_1})$, $S_0 = m\sqrt{s/h_0}\,J_1(2\sqrt{sh_0})$, $S_1 = m\sqrt{s/h_1}\,J_1(2\sqrt{sh_1})$, $Q_0 = m\sqrt{s/h_0}\,Y_1(2\sqrt{sh_0})$, $Q_1 = m\sqrt{s/h_1}\,Y_1(2\sqrt{sh_1})$.

The vertical magnetic field β_z in (3.4) is obtained by solving the depth-averaged (6.1) for the horizontal component $X(x)$, using appropriate boundary conditions for X and its

https://doi.org/10.1017/jfm.2026.11217 Published online by Cambridge University Press

horizontal flux,

$$X(x_L) = \Theta(x_L), \qquad X'(x_R) = \mathrm{i}k_R\, X(x_R). \tag{6.15}$$

These correspond to an inlet condition at the left boundary ($x = x_L < 0$) and an outgoing (Sommerfeld) condition at the right boundary ($x = x_R > x_1$), with $k_R = \omega/\sqrt{gh_R}$, where again the bathymetry smoothly connects to constant-depth regions.

The numerical solution is computed using a shooting method in Mathematica. As an internal consistency check, we report relative residuals $\mathcal{R}_2 = \|L(X)\|_2/\max|X|$, $\mathcal{R}_\infty = \|L(X)\|_\infty/\max|X|$, computed on a uniform grid over the slope. We obtain $\mathcal{R}_2 = O(10^{-10})$ and $\mathcal{R}_\infty = O(10^{-8})$. Similarly, the absolute error related to the enforcement of the radiation condition at the right boundary is $O(10^{-5})$, and the error of the jump conditions at x_0 and x_1 is $O(10^{-13})$. The error analysis therefore confirms that the boundary-value problem is satisfied to high accuracy. Replacing the analytical Θ by a numerical solution would not alter our conclusions since the magnetic field is passive.

Figure 3 shows snapshots of the free-surface elevation (panel a), vertical magnetic field at the seabed (panel b) and depth profile (panel c) for a period of 300 s, with $h_0 = 2000$ m and $m = 0.025$. In the upper panel, the full numerical solution is compared with the analytical free-surface elevation (6.8)–(6.10), showing excellent agreement. Panel (*c*) shows comparison between the depth-averaged and full numerical solutions for the vertical magnetic field at the seabed. The curves are almost indistinguishable, again indicating excellent agreement. The relative L_2 error between the complex depth-averaged and full numerical solutions for β_z at the seabed is $O(10^{-2})$. Similar results are obtained for other mild-slope configurations, such as a gently down-sloping seabed with $m = -0.025$, and are therefore not shown for brevity.

This validation confirms that the depth-averaged formulation provides an accurate representation of the magnetic field when the asymptotic ordering $|\nabla_2 h| \ll kh \ll 1$ is satisfied. Figure 3 shows that, while the maximum free-surface elevation increases by $\sim$20 % as the wave shoals over the slope, the vertical magnetic field decreases by $\sim$5 %. This result reveals that the direct correlation between the free-surface elevation Θ and the vertical magnetic field at the seabed β_z implied by Tyler's formula (3.11) breaks down in varying depth regions. We provide a physical explanation of this phenomenon in the next section.

7. Physical interpretation

Sample computations have been carried out to investigate the behaviour of the magnetic signal in varying water depths, particularly as the water depth decreases and the incident long wave shoals. This aspect has not been extensively studied in the literature and is therefore worth further investigation.

We show that the induced magnetic field is governed by the progressive energy flux, modulated by weak slope-induced reflections. Consider the WKB approximation for slowly varying depth, $\Theta(x) \simeq A_+(x)\exp[\mathrm{i}S(x)] + A_-(x)\exp[-\mathrm{i}S(x)]$, where $S'(x) = k(x)$ and the local amplitudes $A_\pm(x)$ satisfy

$$|A_\pm(x)| = \frac{1}{2}\left|\Theta(x) \pm \frac{\Theta'(x)}{\mathrm{i}k(x)}\right|, \quad |A'_\pm| \ll k|A_\pm|. \tag{7.1}$$

Hence, the forward (right-going) energy flux associated with the forward wave component is $EC_g^+(x) = (1/2)\rho g|A_+(x)|^2\sqrt{gh(x)}$; Mei *et al.* (2005). Now, introduce the flux-response factor

https://doi.org/10.1017/jfm.2026.11217 Published online by Cambridge University Press

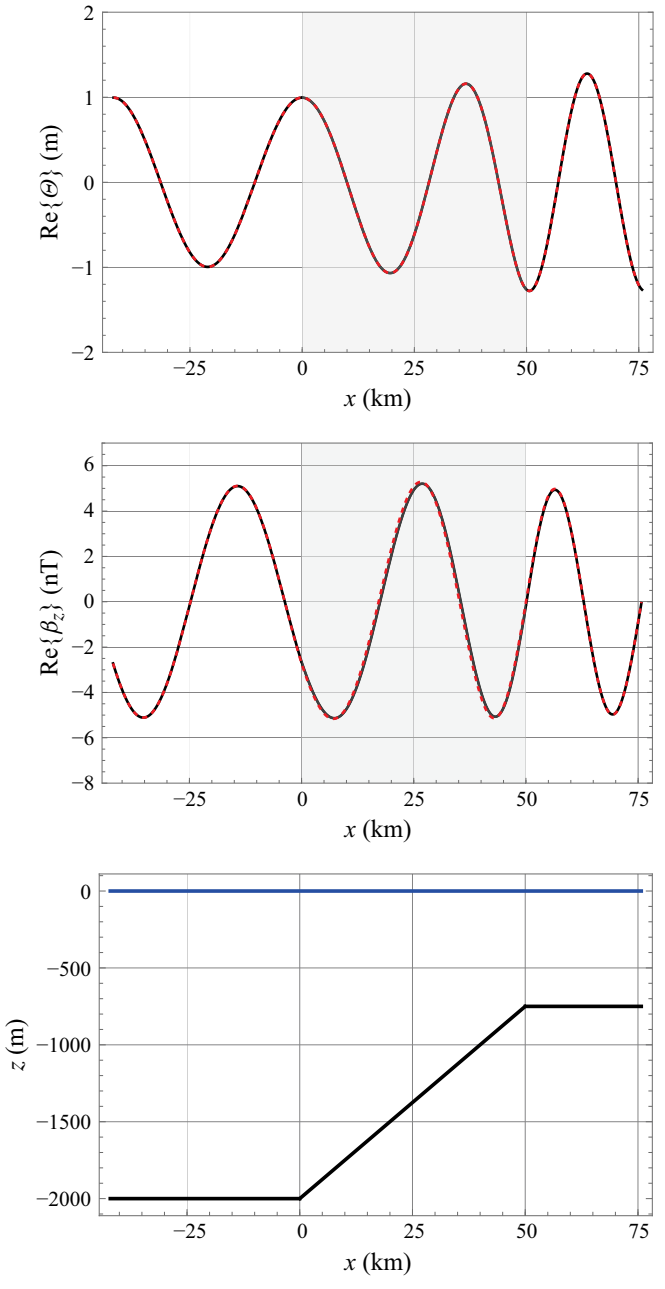


Figure 3. Comparison between analytical and full numerical solutions at $t = 2\pi/\omega$. (*a*) Free-surface elevation, with solid line (–) for the analytical solution (6.8)–(6.10) and red dashed line (- -) for the full numerical solution. (*b*) Vertical magnetic field at the seabed, with solid line (–) for the depth-averaged solution and red dashed line (- -) for the full numerical solution. (*c*) Bottom profile. Shaded regions indicate the shoaling zone.

$$C_F(x) = \frac{|\beta_z(x)|}{EC_g^+(x)} \tag{7.2}$$

defined as the ratio of the vertical magnetic field to the forward wave energy flux. Here, C_F expresses how efficiently an incoming gravity wave forces an induced magnetic signal.

https://doi.org/10.1017/jfm.2026.11217 Published online by Cambridge University Press

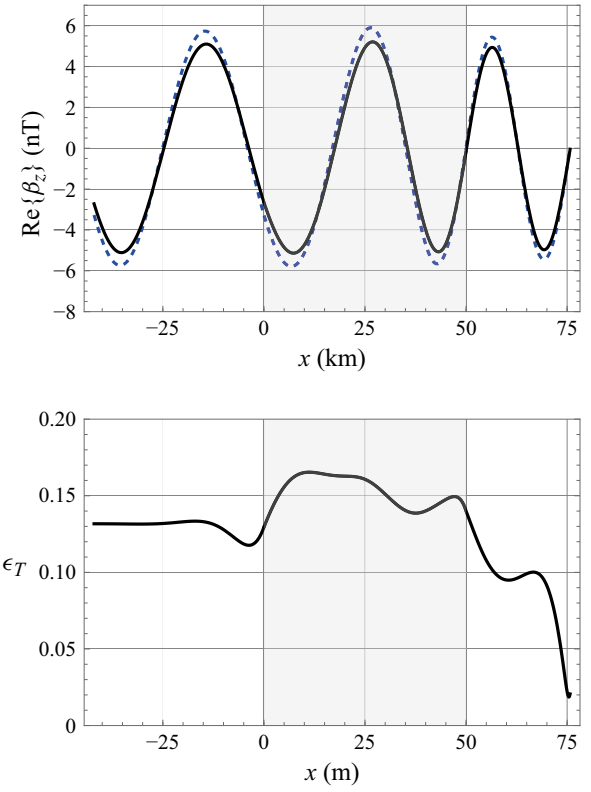


Figure 4. Comparison between depth-averaged and Taylor solutions. (*a*) Vertical magnetic field on the seabed at time $t = 2\pi/\omega$, with solid line (–) for the depth-averaged model and blue dashed line (- -) for the Taylor solution. (*b*) Relative error between full complex Taylor and depth-averaged solutions. Parameters are the same as in figure 3. The shadowed areas represent the shoaling region.

A constant C_F means the induction follows the progressive flux, whereas a varying C_F means the model responds to local kinematics rather than true flux transport.

This definition enables us to introduce the non-dimensional flux-response coefficients

$$R_F^m = C_F^m(x)/C_F^m(\bar{x}), \quad R_F^{\mathrm{T}} = C_F^{\mathrm{T}}(x)/C_F^m(\bar{x}), \tag{7.3}$$

where C_F^m indicates that β_z in (7.2) is calculated using the depth-averaged model, C_F^{T} is calculated with Tyler's formula (3.11) and $\bar{x}$ is a reference point (e.g. in the flat region $x < 0$, some wavelengths away from the slope change). A nearly constant value of R_F indicates that the induced magnetic field scales directly with the progressive energy flux, i.e. induction follows flux conservation as the wave shoals. Variations in R_F quantify departures from this flux-governed behaviour.

Figure 4(*a*) compares the vertical magnetic field at the seabed for the same profile as in figure 3, showing the depth-averaged solution (validated in § 6.3) and the solution given by Tyler's formula (3.11). The relative error ϵ_T, computed on the full complex fields, between the depth-averaged and Tyler solutions is shown in panel (*b*). The differences between the Tyler and depth-averaged solutions are clearly visible, with the relative error reaching a maximum of approximately 17 % at the start of the slope, oscillating approximately 15 % across the variable-depth region, and decreasing in the shallows, where Tyler's approximation becomes more accurate as the conditions approach the limit $kh \to 0$.

https://doi.org/10.1017/jfm.2026.11217 Published online by Cambridge University Press

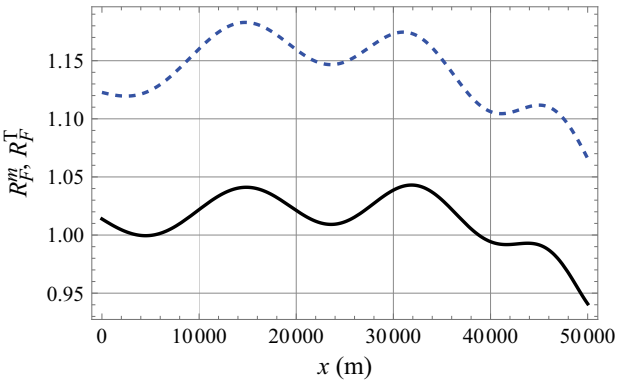


Figure 5. Coefficients R_F^m and R_T^m over the shoaling region, corresponding to the magnetic field shown in figure 4.

Finally, figure 5 shows R_F^m and R_F^{T} over the sloping region. Across the variable-depth region, the flux-normalised response from the depth-integrated model remains close to unity, with R_F^m oscillating weakly around 1.03. This indicates a modest ($\sim$3 %) departure from a fully flux-governed regime, with the oscillations attributable to weak slope-induced reflections and interference. By contrast, Tyler's approximation yields a substantially larger response, $R_F^{\mathrm{T}} \approx 1.15$, implying a systematic overestimation of order 10 % relative to the depth-integrated solution.

The present results show that, over mild slopes, the induced magnetic field is governed primarily by the progressive energy flux of the incident long wave. In the depth-integrated formulation, the magnetic field follows this flux propagation, so that the flux-response coefficient remains nearly constant as the wave shoals, apart from small modulations likely associated with weak reflections. In contrast, Tyler's locally kinematic approximation (3.11) links the magnetic field directly to the local surface amplitude and depth, without accounting for the transport of energy flux. As a result, it overestimates the magnetic response on slopes, where the local amplitude increases while the forward flux decreases (Mei *et al.* 2005).

8. Parametric analysis

We perform a parametric analysis to investigate the range of validity of the depth-averaged and Tyler solutions. To parametrise the study, we introduce three non-redundant non-dimensional groups. First, the long-wave parameter $\delta_0 = k_0 h_0$ captures the effect of varying the period (and hence, the wavenumber through the dispersion relation). The subscript denotes quantities evaluated at a reference point where the seabed is flat (typically on the upstream side of the computational domain) used as the spatial baseline for non-dimensionalisation. Second, the mild-slope parameter $\epsilon_0 = |\nabla h|/\delta_0$ quantifies the spatial variation of the seabed relative to the dispersion parameter and, hence, the regime of validity of the depth-integrated approximation. Third, the bathymetric contrast $\gamma = h_{\min}/h_{\max}$ specifies the overall shoaling strength.

To focus on the mild-slope dependence, we fix the bathymetric strength at $\gamma = 0.5$, corresponding to a 50 % reduction in depth across the slope. This choice provides a balanced configuration, sufficiently strong to reveal the effect of topography, while remaining within the asymptotic regime investigated here. Three representative values of the upstream mild-slope parameter are considered, $\epsilon_0 = \{0.05,\ 0.10,\ 0.20\}$, capturing the

https://doi.org/10.1017/jfm.2026.11217 Published online by Cambridge University Press

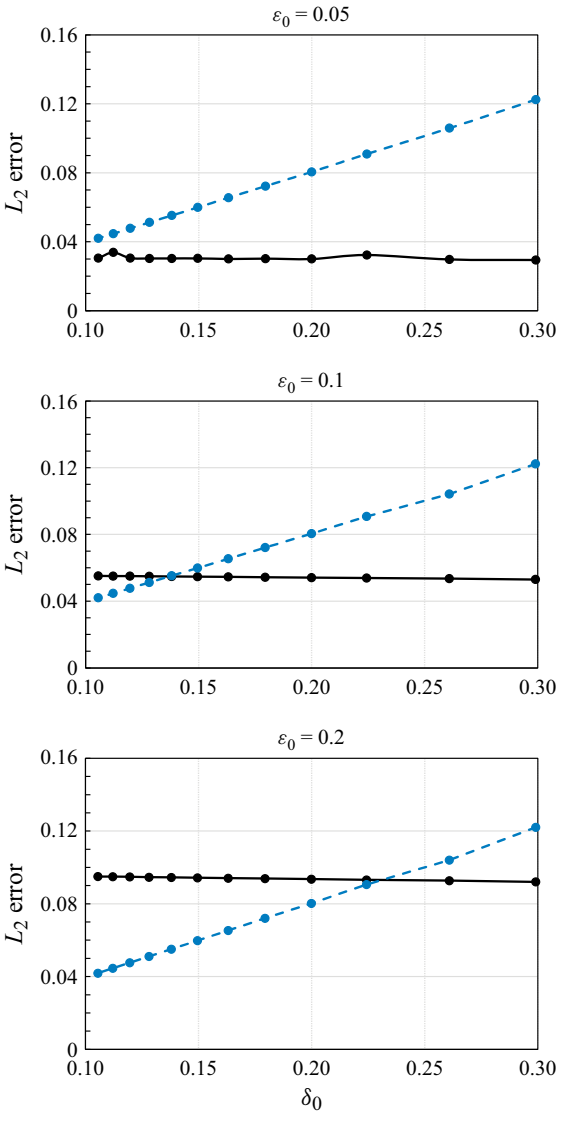


Figure 6. Relative L_2 error of the depth-averaged solution (–) and Tyler's formula (- -) versus dispersion parameter δ_0 for $\epsilon_0 = \{0.05, 0.1, 0.2\}$ and $\gamma = 0.5$.

transition from weak to moderate topographic influence, while the long-wave parameter is varied in the range $\delta_0 \in [0.1,\ 0.3]$.

Figure 6 shows the relative L_2 error between the depth-averaged and Tyler solutions with respect to the full numerical model. In all cases, the depth-averaged error remains nearly constant as δ_0 increases, exhibiting only small oscillations, whereas the Tyler error grows almost linearly with δ_0. For $\epsilon_0 < 0.2$, the depth-averaged formulation outperforms Tyler's for almost all δ_0, achieving an L_2 error of $O(10^{-2})$. At $\epsilon_0 = 0.2$, the mild-slope assumption is effectively exhausted and Tyler's local approximation becomes more accurate almost everywhere, as expected when the depth-averaged closure begins to lose asymptotic validity.

https://doi.org/10.1017/jfm.2026.11217 Published online by Cambridge University Press

These results reveal a previously unrecognised physical regime for tsunami-induced magnetism, in which the electromagnetic field is governed by the progressive transport of wave energy rather than by the local free-surface motion. The depth-averaged formulation captures this flux-driven behaviour and thus extends the classical Tyler theory, which neglects it, providing the first quantitative boundary of asymptotic validity at $\epsilon < 0.2$.

9. Conclusions

We have derived, implemented and tested a depth-averaged model of the magnetic anomalies induced by long surface waves propagating over variable bathymetry. The formulation is monochromatic and frequency domain: all quantities represent steady-state complex amplitudes of a long-wave component with frequency ω, so temporal and spectral decompositions are implicit in the solution. A full time-domain response can be reconstructed by superposing such monochromatic components, i.e. by convolving the present frequency-domain solution with the temporal spectrum of an arbitrary incident wave packet (Renzi & Mazza 2023).

The formulation is computationally efficient, asymptotically consistent with the constant-depth theory and captures shoaling effects that are absent from Tyler's local approximation. Crucially, the analysis demonstrates that the magnetic field induced by a shoaling long wave is governed by the progressive transport of wave energy rather than by the local surface amplitude. This flux-driven mechanism defines a new physical regime for tsunami-induced magnetism and explains why the magnetic signal can attenuate even as the free-surface elevation increases.

The analysis is conducted in a local Cartesian frame, appropriate for regional scales where the horizontal extent $L \ll R_{\mathrm{E}}$, where R_E is Earth's radius. For typical wavelengths ($L \lesssim 300\,\mathrm{km}$), curvature effects scale as $O(L/R_{\mathrm{E}}) \sim 10^{-2}$ and are therefore negligible at the present level of approximation. A fully spherical formulation would be required only for global-scale coupling, which is outside the scope of this work.

Finally, we remark that the novel depth-averaged formulation derived in this work is valid under the long-wave approximation $\delta \ll 1$. The approach of Wang & Liu (2013) provides a natural higher-order extension that could be incorporated in future work to explore dispersive corrections to the magnetic response.

The results provide a quantitative bridge between simplified analytical theory and full electromagnetic simulations, offering a physically consistent and computationally tractable framework for interpreting seafloor and satellite magnetic observations.

Funding. J.S.Z. was supported by PRINT/UFRGS-CAPES (Brazil).

Declaration of interests. The authors report no conflict of interest.

Appendix A. Analytical evaluation of integrals in (4.9)

Here, we detail the analytical expressions for the integrals in (4.10),

$$A(h) = \int_{-\infty}^{+\infty} f^2 \,\mathrm{d}z = -\Big\{F_z^2 g^2 k^3 \big[k^2 \sinh(\alpha h)\big(2\alpha^2 h - 3k\big) + \alpha \cosh(\alpha h) \times \big(k^2(hk-4) + \alpha^2(hk+1)\big) + 2\alpha k^2(hk+2) - \alpha^3(hk+1)\big]\Big\} \times \left\{2\alpha^5 \eta^2 \omega^2 \left[\alpha \sinh\left(\frac{\alpha h}{2}\right) + k \cosh\left(\frac{\alpha h}{2}\right)\right]^2\right\}^{-1}, \tag{A1}$$

https://doi.org/10.1017/jfm.2026.11217 Published online by Cambridge University Press

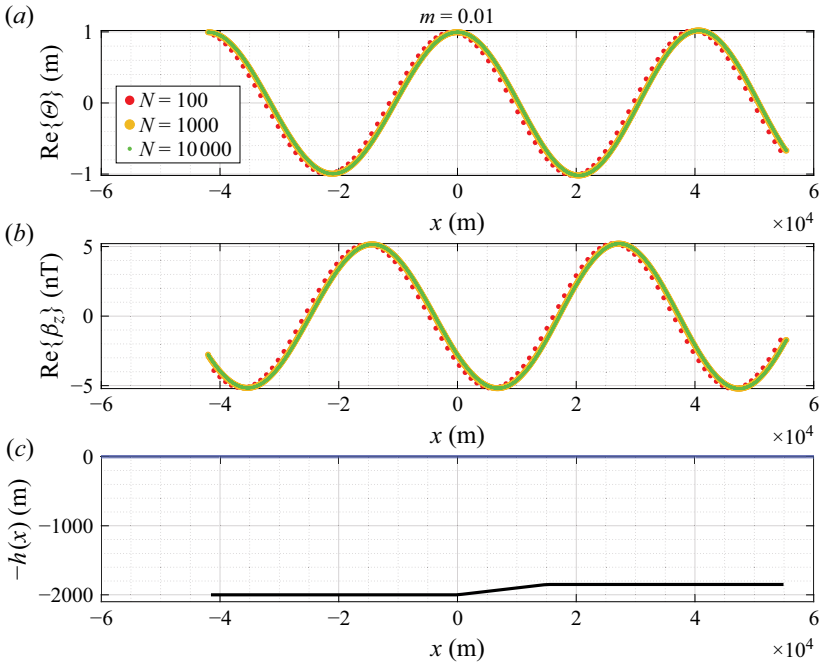


Figure 7. Plots of the (*a*) free-surface elevation, (*b*) vertical magnetic field at the seabed and (*c*) depth profile for $m = 0.01$, $h_0 = 2000$ m, $F_z = -20\,000$ nT, $\eta = 198\,944$ m^2 s^{-1} and a period of 300 s.

$$B(h) = \int_{-\infty}^{+\infty} f \frac{\partial f}{\partial h}\, \mathrm{d}z = -\left\{ F_z^2 g^2 k^4 \left[\alpha \cosh\left(\frac{\alpha h}{2}\right) + k \sinh\left(\frac{\alpha h}{2}\right) \right] \left[\left(\alpha^2 + k^2\right) \sinh(\alpha h) - \alpha k(-2\cosh(\alpha h) + hk + 2) \right] \right\} \left\{ 4\alpha^4 \eta^2 \omega^2 \left[\alpha \sinh\left(\frac{\alpha h}{2}\right) + k \cosh\left(\frac{\alpha h}{2}\right) \right]^3 \right\}^{-1}, \tag{A2}$$

$$C(h) = \int_{-h}^{0} f\, \mathrm{d}z = -\frac{\mathrm{i} F_z g k^2 \left[\sinh\left(\frac{\alpha h}{2}\right) \left(\alpha^2 h - 2k\right) + \alpha h k \cosh\left(\frac{\alpha h}{2}\right) \right]}{\alpha^3 \eta \omega \left[\alpha \sinh\left(\frac{\alpha h}{2}\right) + k \cosh\left(\frac{\alpha h}{2}\right) \right]}. \tag{A3}$$

Appendix B. Numerical analysis

The linearly varying bottom profile $h(x) = h_0 - mx$ is adopted as a canonical configuration for testing the numerical model. A grid-refinement study was carried out for representative bottom slopes $m = \{0.01,\ 0.1\}$, using $N = \{10^2,\ 10^3,\ 10^4\}$ grid points. Figures 7–8 show the corresponding sensitivity plots of the free-surface amplitude Θ and the induced magnetic field β_z.

The solutions obtained with $N = 10^3$ and $N = 10^4$ points are indistinguishable, whereas the coarse grid ($N = 10^2$) shows a small but noticeable deviation. To quantify convergence, the relative L_2 and L_∞ norms of the difference between successive resolutions were

https://doi.org/10.1017/jfm.2026.11217 Published online by Cambridge University Press

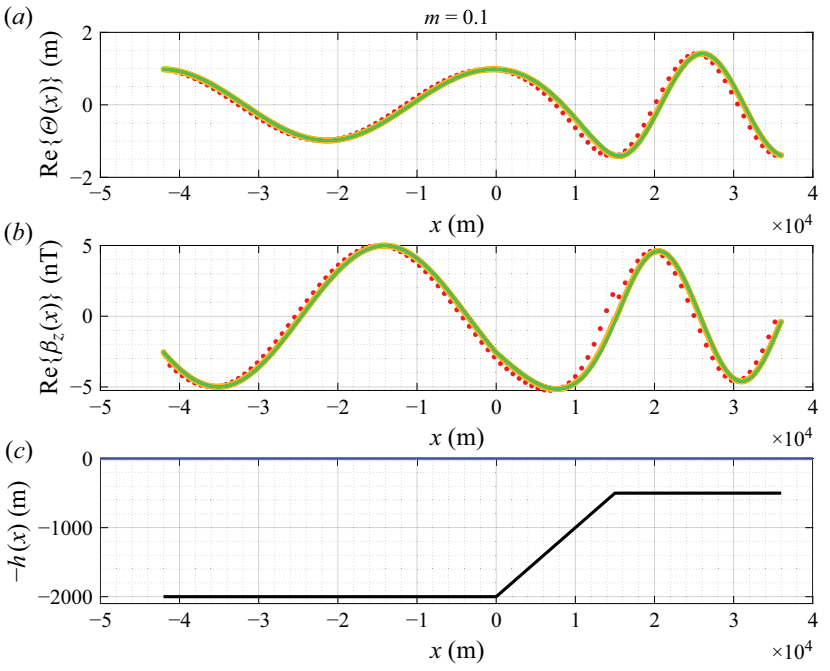


Figure 8. Plots of the (*a*) free-surface elevation, (*b*) vertical magnetic field at the seabed and (*c*) depth profile for $m = 0.1$. Other parameters are as in figure 7.

computed after interpolating all solutions onto the finest grid, and the observed convergence rate was estimated as

$$p = \frac{\log(E_{12}/E_{23})}{\log(\rho)}, \tag{B1}$$

where $\rho = 10$ is the refinement ratio and E_{ij} denotes the normed difference between solutions at successive resolutions. For all tested slopes, the results give $p \simeq 1.0$ for both Θ and β_z, indicating first-order accuracy of the numerical method. The first-order behaviour is consistent with the stepwise representation of the bottom profile and the corresponding first-order treatment of the slope transition. The relative error between the two finest grids is below 1 % in all cases, confirming that the solution obtained with $N = 10^4$ points is grid-independent for the purposes of this study.

References

Abdolali, A., Kirby, J. & Bellotti, G. 2015 Depth-integrated equation for hydro-acoustic waves with bottom damping. *J. Fluid Mech.* **766**, R1.

Davidson, P.A. 2016 *Introduction to Magnetohydrodynamics*. Cambridge University Press.

Devillard, P., Dunlop, F. & Souillard, B. 1988 Localization of gravity waves on a channel with random bottom. *J. Fluid Mech.* **186**, 521–538.

Dingemans, M.W. 1997 *Water Wave Propagation Over Uneven Bottoms*. World Scientific.

Evans, D.V. & Linton, C.M. 1994 On step approximations for water-wave problems. *J. Fluid Mech.* **278**, 229–246.

Galtier, S. 2016 *Intdroduction to Modern Magnetohydrodynamics*. Cambridge University Press.

Mei, C.C., Stiassnie, M. & Yue, D.K.-P. 2005 *Theory and Applications of Ocean Surface Waves*. World Scientific.

Miller, S., Renzi, E. & Discacciati, M. 2025 Taylor consistent discretisation of the Laplace operator in the moving particle semi-implicit method. *J. Comput. Appl. Maths* **475**, 117000.

https://doi.org/10.1017/jfm.2026.11217 Published online by Cambridge University Press

MINAMI, T. & TOH, H. 2013 Two-dimensional simulations of the tsunami dynamo effect using the finite element method. *Geophys. Res. Lett.* **40**, 4560–4564.

MINAMI, T., TOH, H., ICHIHARA, H. & KAWASHIMA, I. 2017 Three-dimensional time domain simulation of tsunami- generated electromagnetic fields: application to the 2011 Tohoku earthquake tsunami. *J. Geophys. Res. Solid Earth* **122**, 9759–9779.

MINAMI, T., TOH, H. & TYLER, R.H. 2015 Properties of electromagnetic fields generated by tsunami first arrivals: classification based on the ocean depth. *Geophys. Res. Lett.* **42**, 2171–2178.

MOREAU, R. 1990 *Magnetohydrodynamics*. Springer.

RENZI, E. & MAZZA, M.G. 2023 Electromagnetic field generated by tsunamigenic seabed deformation. *J. Fluid Mech.* **966**, A3.

SAMMARCO, P., CECIONI, C., BELLOTTI, G. & ABDOLALI, A. 2013 Depth-integrated equation for large-scale modelling of low-frequency hydroacoustic waves. *J. Fluid Mech.* **722**, R6.

TATEHATA, H., ICHIHARA, I. & HAMANO, Y. 2015 Tsunami-induced magnetic fields detected at Chichijima Island before the arrival of the 2011 Tohoku earthquake tsunami. *Earth Planets Space* **67**, 185.

TOH, H., SATAKE, K., HAMANO, Y., FUJII, Y. & GOTO, T. 2011 Tsunami signals from the 2006 and 2007 Kuril earthquakes detected at a sea-floor geomagnetic observatory. *J. Geophys. Res.* **116**, B02104.

TYLER, R.H. 2005 A simple formula for estimating the magnetic fields generated by tsunami flow. *Geophys. Res. Lett.* **32**, L09608.

WANG, B. & LIU, H. 2013 Space–time behaviour of magnetic anomalies induced by tsunami waves in open ocean. *Proc. R. Soc. Lond. A* **469**, 20130038.

https://doi.org/10.1017/jfm.2026.11217 Published online by Cambridge University Press